Check for updates

Au nanoparticle sensitized blue TiO$_2$ nanorod arrays for efficient Gatifloxacin photodegradation†

Jun Guo, [ab] Wei Gan,[b] Ruixin Chen,[b] Miao Zhang [*b] and Zhaoqi Sun*[b]

TiO$_2$ nanorod arrays have been widely used in photocatalytic processes, but their poor visible light absorption and rapid carrier recombination limit their application. Both introducing oxygen vacancies and using precious metals as surface plasmon resonance (SPR) stimulators are effective strategies to enhance their photocatalytic performance. Herein, Au nanoparticle sensitized blue TiO$_2$ nanorod arrays (Au/B-TiO$_2$) were successfully fabricated for efficient Gatifloxacin photodegradation. The degradation efficiency of Gatifloxacin was up to 95.0%. Moreover, the corresponding reaction rate constant (K_a) was up to 0.02007 min^{-1}. Additionally, it was suggested that Gatifloxacin could be subject to three different degradation pathways. The superior catalytic activity of Au/B-TiO$_2$ is a result of the combined effect of the two components. Firstly, TiO$_2$ nanorod arrays provide a larger surface area for Au deposition and act as efficient transfer channels. Secondly, the presence of oxygen vacancies in blue TiO$_2$ nanorod arrays enhances the catalytic activity. Thirdly, Au acts as a SPR activator, providing a large number of high-energy electrons in the photocatalysis process. Lastly, the improved light capture capabilities are essential for efficient removal of Gatifloxacin. This work provides a new approach for the construction of a high-performance heterojunction photocatalyst in advanced oxidation processes.

1. Introduction

Antibiotics are commonly used to treat a variety of illnesses; Gatifloxacin, a fourth-generation fluoroquinolone, being one of the most popular.[1,2] However, due to its toxicity, it is not easily removed from wastewater during the treatment process, leading to the accumulation of Gatifloxacin in natural water bodies and causing issues such as bacterial resistance and water pollution.[3,4] Advanced oxidation processes (AOPs) are an effective way to remove antibiotic contaminants from wastewater by using highly active free radicals. Photocatalysis is a particularly popular AOP due to its efficient use of solar energy and its cycle stability, making it an economical and environmentally friendly option.[5–7]

Titanium dioxide (TiO$_2$) is a popular semiconductor photocatalytic material because of its stability, non-toxicity, and low cost. But two major challenges remain: its low visible light absorption ability due to its wide band gap of 3.0–3.2 eV, and the rapid recombination of carrier pairs due to a large number of defects in the crystal centre.[8,9] To address these issues, numerous approaches have been attempted to develop highly active photocatalysts that can absorb more visible light and

have low carrier recombination rates.[10,11] In recent years, researchers have identified and demonstrated that numerous defective metal-oxide semiconductors containing oxygen vacancies, such as TiO$_2$,[12,13] ZnO,[14] CeO$_2$,[15] and WO$_3$ (ref. 16) exhibit superior catalytic reactivity. These materials have been utilized in various photochemical energy conversions, including photocatalytic H$_2$O$_2$ production, pollutant removal, CO$_2$ reduction, CO oxidation, and water splitting. The oxygen vacancies in these materials can adjust the band structure, lower the band gap, enhance carrier separation and facilitate charge transfer, leading to enhanced catalytic activity.[17–19]

By activating persulfate (PS) with a blue-TiO$_2$ nanotube anode under electrochemical conditions, Zhou's team discovered that it is possible to decompose 2,4-dichlorophenoxyacetic acid efficiently while consuming minimal energy.[20] Lee and colleagues discovered that the photooxidation of hazardous NO gas by blue TiO$_2$ nanoparticles doped with Sn can be utilized as an effective atmospheric pollution remediation agent, achieving an efficiency of 72% in 60 min when exposed to sunlight.[21] According to Kumar' research, blue TiO$_2$ nanorods modified with porous g-C$_3$N$_4$ had a remarkable capacity to convert CO$_2$ to solar fuel, with an efficiency of up to 92%.[22] Xu *et al.*'s research revealed that the blue-TiO$_2$/PbO$_2$-carbon nanotube electrode could completely oxidize 100 mg L^{-1} phenol in 210 min, offering a promising option for the purification of wastewater with phenol.[23] Moreover, it has been demonstrated that a blue TiO$_2$ nanotube array as an anode is successful in degrading 2,4-dichlorophenoxyacetic acid through a photocatalytic/photofenton process, thus providing

^{a}*School of Electronic Engineering, Huainan Normal University, Huainan, 232038, P. R China*

^{b}*School of Materials Science and Engineering, Anhui University, Hefei, 230601, P. R China. E-mail: zhmiao@ahu.edu.cn; szq@ahu.edu.cn*

a potential solution for the disposal of herbicide-containing wastewater.[24] In addition, a blue TiO_2 photocatalyst, which was supported by photonic crystals, was observed to have a higher CO_2 photoreduction activity and improved CH_4 selectivity.[25]

Defect engineering can improve the catalytic efficiency of TiO_2, but it is still not able to effectively absorb and utilize the visible light which comprises the majority of the solar energy.[26] To further amplify the visible light absorption of TiO_2, surface plasmon resonance (SPR) metals have been incorporated, which widens the range of light absorption and provides more active sites to boost the photocatalytic process, thereby supplying hot electrons to the semiconductor, diminishing carrier recombination, and ultimately improving carrier separation.[27–29] Au, as a typical SPR metal, has been shown to be an important factor in the photocatalytic performance of TiO_2.[30] Researchers have demonstrated that Au/TiO_2 nanoparticles have good catalytic activity in both thermal and photocatalytic CO_2 conversion.[31] Furthermore, due to the SPR excited state charges, Au/TiO_2 nanostructures have been proven to be beneficial for photochemical (PEC) water splitting and organic pollutant photodegradation.[32] It has been observed that the $TiO_2/Au/TiO_2$ sandwich-type plasma photocatalysts display improved photocatalytic activity and durability when subjected to visible light.[33] Additionally, Rebrov's team discovered that Au/TiO_2 can efficiently photo-catalyze the reduction of 4-nitrophenol to 4-aminophenol under green light.[34] Au nanorods were also used to modify TiO_2 nanobelts in order to improve the light absorption of the full solar spectrum for efficient photocatalytic antibacterial activity applications.[35] In conclusion, combining blue TiO_2 and plasma Au is an effective method to produce high-performance photocatalysts.

In this work, a novel heterostructure catalyst ($Au/B-TiO_2$) was developed for efficient removal of Gatifloxacin by means of Au sensitized blue TiO_2 nanorod arrays. The photocatalytic properties of the catalyst were studied and the degradation pathway and catalytic mechanism of Gatifloxacin were investigated. This research provides potential for the creation of novel heterojunction catalysts and a better comprehension of the pathways and mechanisms of Gatifloxacin decomposition.

2. Experimental

2.1 Materials

Gatifloxacin, chloroauric acid ($HAuCl_4$), sodium borohydride ($NaBH_4$), sulfate (Na_2SO_4), and p-benzoquinone (BQ) were procured from Aladdin Biochemical Technology Co., Ltd. FTO glasses were purchased from Wu Han Jinge Solar Energy Technology Co., Ltd. Ethylenediaminetetraacetic acid disodium (EDTA–2Na), sodium sulfide (Na_2S), and sodium sulfite (Na_2SO_3) were sourced from Beijing Innochem Science & Technology Co., Ltd. Hydrochloric acid (HCl) and isopropyl alcohol (IPA) were obtained from Sinopharm Chemical Reagent Co., Ltd.

2.2 Production of $Au/B-TiO_2$

The TiO_2 nanorod arrays were prepared by traditional hydrothermal process.[36] The precursor solution was prepared by combining deionized water, hydrochloric acid and tetrabutyl titanate in a ratio of 15 : 15 : 0.5. Subsequently, the solution was put into a Teflon reactor containing FTO glass and heated at 150 °C for 720 min. The nanorod arrays were then cleaned and dried for future use. To obtain blue TiO_2 ($B-TiO_2$) with oxygen vacancies defect, $NaBH_4$ treatment was performed.[12] A piece of TiO_2 nanorod arrays (3×2 cm^2) placed in a ceramic kettle, then it was completely covered with ground $NaBH_4$ powder. This was then transferred to a tube furnace for thermal reduction treatment in a N_2 atmosphere. The temperature was set to 340 °C and the process was completed in 120 min. Au nanoparticles were then modified on $B-TiO_2$ by photoreduction of $HAuCl_4$.[37] $B-TiO_2$ was immersed in $HAuCl_4$ solution with a concentration of 0.6 mg mL^{-1}, and then irradiated under a 39 W mercury lamp for 10, 30, and 60 min to produce $Au/B-TiO_2$-1, $Au/B-TiO_2$-2, and $Au/B-TiO_2$-3, respectively. Finally, they were given a thorough cleaning and dried, in preparation for further use. Fig. 1 illustrates the steps involved in the preparation process.

2.3 Characterizations

An X-ray diffractometer (XRD) from Empyrean S, which utilized Cu Kα radiation, was utilized to obtain XRD data, and a Hitachi-S4800 instrument was used to obtain scanning electron microscopy (SEM) images. For Transmission electron microscopy (TEM) and high-resolution TEM (HRTEM), a Fei-2000 was employed. Additionally, X-ray photoelectron spectroscopy (XPS; ESCALAB-250) was utilized to investigate chemical states, and Electron spin resonance (ESR) measurements were executed utilizing an EMX+ (Bruker).

2.4 Optical and photoelectrochemical investigations

A Shimadzu UV-2550 spectrophotometer was employed to acquire the absorption spectra. To measure photoluminescence (PL) spectra, a Hitachi FL-4500 fluorescence spectrophotometer was utilized. The CHI660D electrochemical workstation, comprising a three-electrode system, was used to record the photocurrent response, electrochemical impedance spectroscopy (EIS) and Mott–Schottky curves. The photocurrent response test was conducted using the Zolix LSH-X500 irradiation source that had a power of 500 mW cm^{-2}. Furthermore, a combination of 0.25 M Na_2S and
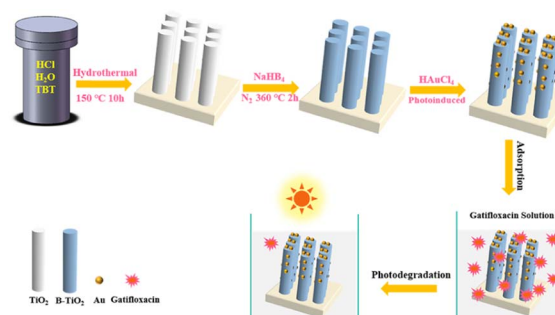

Fig. 1 Diagram of preparation of $Au/B-TiO_2$ system and its photocatalytic process.

0.35 M Na_2SO_3 was used as the electrolyte of EIS, and a 0.1 M Na_2SO_4 solution was utilized for the photoelectric response and Mott–Schottky test.

2.5 Photodegradation analysis

To evaluate the photodegradation of various samples (2×2 cm^2), 10 mL of Gatifloxacin (10 mg L^{-1}) was exposed to a 300 W xenon lamp. A dark adsorption period of 30 min was conducted before the light was switched on, to reach absorption equilibrium. LCMS (LTQ Orbitrap XL) was utilized to analyse the decomposition intermediates. An LC-MS was employed with a C18 analytical column, and the liquid flow phases were composed of water and methane. Data acquisition was done in the m/z range of 50–500. The Shimadzu TOC-L CPH was utilized to carry out a Total Organic Carbon (TOC) test.

3. Results and discussion

3.1 Microstructure investigations

The XRD spectra of all samples are displayed in Fig. 2a, showing seven clear characteristic peaks. The peaks at 36.1°, 41.3°, 54.2°, 62.8°, and 69.8° are linked to the (101), (111), (211), (002), and (112) crystal planes of rutile TiO_2 respectively, as per JCPDS No. 21-1276. Referring to JCPDS No. 65-2870, the remaining two peaks at 38.2° and 44.4° belong to the (111) and (200) crystal planes of Au, respectively.[38] The corresponding optical images of all samples are shown in Fig. 2b.

The surface SEM images of TiO_2 and B-TiO_2, presented in Fig. S1,† demonstrate the dimensions of the TiO_2 nanorod arrays to be between 140–200 nm. In addition, Fig. 3a represents the SEM image of Au/B-TiO_2-2, and it is evident that a large amount of Au nanoparticles has been successfully modified on the TiO_2 nanorod arrays, and the sizes of the Au nanoparticles are between 40–80 nm. HRTEM images in Fig. 3b and c show that the crystal face spacing of 0.25 nm is associated with the (101) plane of rutile TiO_2, while the 0.24 nm crystal face spacing corresponds to Au(111).[39] These findings are corroborated by the XRD results (Fig. 2a). The element mapping diagram (Fig. 3d) confirms the successful synthesis of Au/B-TiO_2.
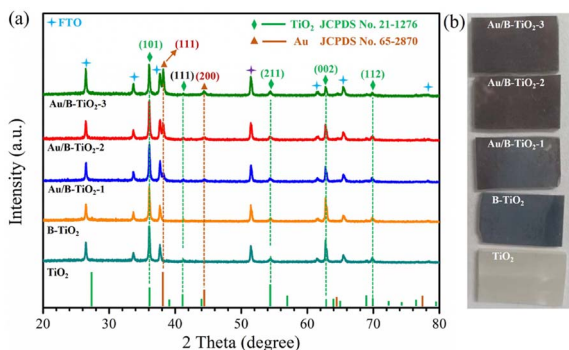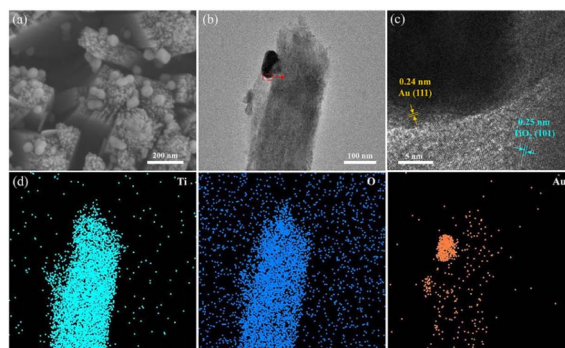

Fig. 3 (a) SEM image of Au/B-TiO_2-2, and its (b) TEM image, (c) HRTEM image, and (d) elemental mappings, respectively.

3.2 XPS investigations

Verification of the chemical states of Au/B-TiO_2-2 was conducted using XPS. The survey is displayed in Fig. 4a, displaying the presence of Au 4f, Ti 2p and O 1s, demonstrating the coexistence of Au, Ti, and O. As demonstrated by Fig. 4b, two distinct peaks at 83.0 eV and 86.7 eV, belonging to Au $4f_{7/2}$ and Au $4f_{5/2}$, respectively, showing the presence of Au nanoparticles.[26] As shown in Fig. 4c, the Ti 2p spectrum is composed of four distinct peaks at 457.4, 458.4, 463.4, and 464.2 eV, which correspond to Ti^{3+} $2p_{3/2}$, Ti^{4+} $2p_{3/2}$, Ti^{3+} $2p_{1/2}$; and Ti^{4+} $2p_{1/2}$, respectively.[40] The findings indicate the presences of Ti^{3+} and oxygen vacancies in the composite.[12] Fig. 4d presents the O 1s spectra that is composed of three distinct peaks at 529.6, 531.5 and 533.4 eV, respectively. Ti_2O is represented by the 529.6 eV peak, with the 531.5 eV peak being caused by the surface –OH. The third peak at 533.4 eV is caused by the adsorption of H_2O on the surface.[12]

3.3 Optical and photoelectrochemical characteristics

The UV-vis absorption spectra were unitized examining the light capture efficiency of each synthesized sample, as depicted in Fig. 5a. Observation revealed that the bandgap of TiO_2 (3.03 eV)
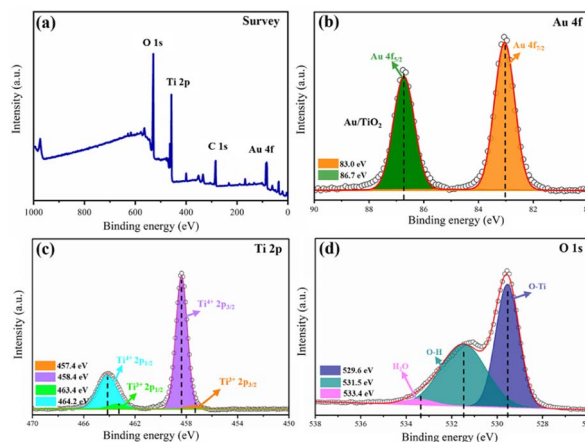

Fig. 2 (a) XRD patterns of each sample, and (b) corresponding optical images.

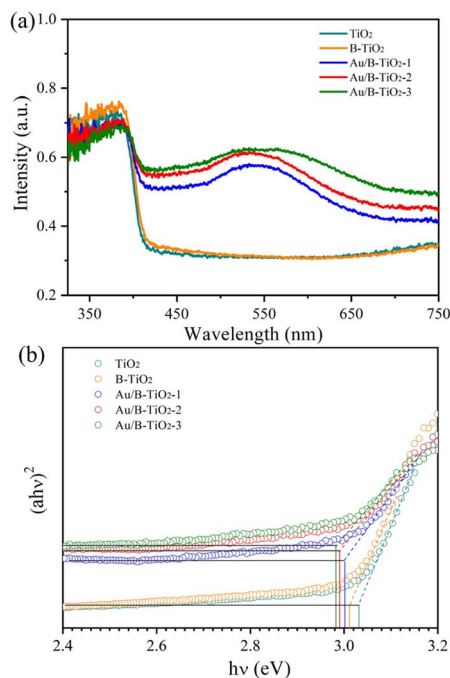**Fig. 4** (a) XPS survey of Au/B-TiO_2-2, and its spectra of (b) Au 4f, (c) Ti 2p, and (d) O 1s.

Fig. 5 (a) UV-vis spectra of each sample, and (b) band gaps.

resulted in a diminished absorption strength for wavelengths less than 400 nm. However, the presence of O vacancies in B-TiO$_2$ increased the absorption strength. Additionally, the sensitization of Au nanoparticles caused the absorption edge to be redshifted and a peak to be observed near 535 nm due to the SPR effect of Au. According to the Tauc equation,[41] the bandgaps (E_g) of TiO$_2$, B-TiO$_2$, Au/B-TiO$_2$-1, Au/B-TiO$_2$-2 and Au/B-TiO$_2$-3 are 3.03, 3.01, 3.00, 2.99 and 2.98 eV, respectively (Fig. 5b). The Au/B-TiO$_2$ system's impressive light absorption capacity implies its effectiveness in photocatalysis.

The efficiency of carrier separation and transport at the interface of various samples were investigated using photoluminescence (PL). To enhance the catalytic performance of the catalyst, it is necessary to reduce the recombination of photogenerated carriers. A weak PL spectrum indicates fewer carrier pairs recombining, which suggests that more carriers are taking part in the catalytic reaction. Fig. 6 demonstrated
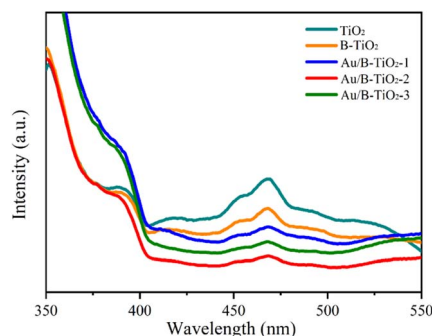
that TiO$_2$ had the most intense PL peak, which implied the highest rate of carrier recombination. Additionally, the presence of oxygen vacancies leaded to a lower peak intensity of B-TiO$_2$ in comparison to TiO$_2$. Further, when Au was added to form Au/B-TiO$_2$, the intensity was further reduced. The PL strength of Au/B-TiO$_2$-2 is the weakest, showing that the recombination of photogenerated carrier pairs is minimized and thus, effective charge separation is achieved.

Moreover, the photochemical properties of the samples were studied using the photoelectric method which revealed that Au/B-TiO$_2$-2 had the highest current density of 25.4 μA cm^{-2}, 3 times more than B-TiO$_2$ and 6.2 times more than TiO$_2$ (Fig. 7a). This suggests that Au/B-TiO$_2$ has a higher carrier separation efficiency, leading to better photodegradation performance.

In addition, the electrochemical impedance spectroscopy (EIS) spectra are presented in Fig. 7b, and it is evident that the Au/B-TiO$_2$-2 sample has the smallest radius, indicating the lowest interfacial charge transport resistance and the highest charge transfer ability.

3.4 Optical and photocatalytic analysis

The photocatalytic performance of all samples was assessed by Gatifloxacin decomposition. The UV–vis spectra of Gatifloxacin solution are represented by Fig. S2,† which vary according to the irradiation time, indicating that Gatifloxacin is gradually removed with increasing light exposure. Fig. 8a illustrates the photodegradation efficiency of Gatifloxacin for various samples. After 150 min, TiO$_2$ had the lowest removal rate of 50.4%. For B-TiO$_2$, the photodegradation efficiency increased to 58.6%. The incorporation of Au further improved the photocatalytic efficiency, with Au/B-TiO$_2$-2 achieving the
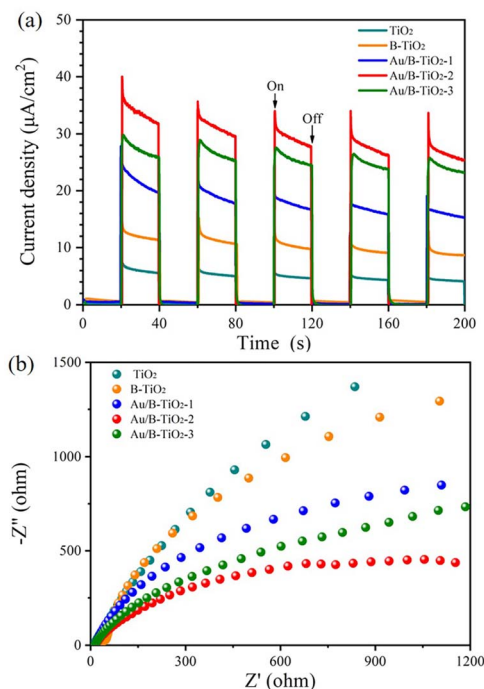

Fig. 7 (a) I–T curves, and (b) EIS curves of each sample.

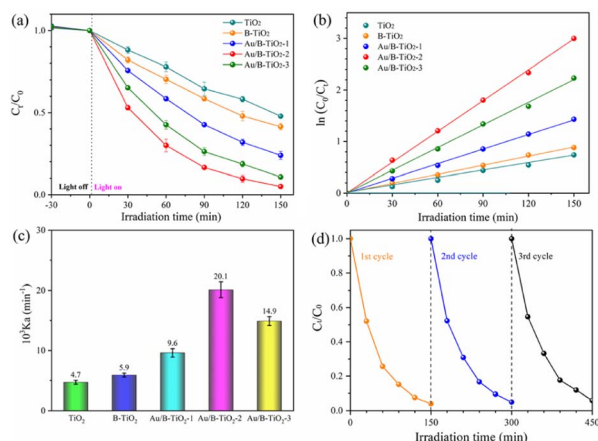Fig. 6 PL spectra of various samples.

Fig. 8 (a) Photodegradation performance of each sample, (b) kinetics fitting, (c) reaction rate constant, and (d) three-cycle test of Au/B-TiO$_2$-2.

highest rate of 95.0%. This improvement is a result of the combined effect of the components, which reduces the interface charge transfer resistance and enhances catalytic efficiency.[17] Secondly, precious metal Au nanoparticles can significantly boost their capacity to absorb visible light through surface plasmon resonance (SPR) effect. Furthermore, as an exceptional provider of plasma electrons, Au can supply an abundance of high-energy electrons into the semiconductor TiO$_2$ in the photocatalytic process.[27] Additionally, TiO$_2$ nanorod arrays facilitate electron transport, thereby contributing to the increased photocatalytic efficiency.

The degradation kinetics curve of Gatifloxacin, shown in Fig. 8b, is linear, indicating that it follows the first-order kinetic law. Fig. 8c displays the reaction rate constants (K_α) of each sample, with TiO$_2$ and B-TiO$_2$ being 0.00740 and 0.00588 min^{-1}, respectively. The highest K_α value is found in Au/B-TiO$_2$-2, which is 4.29 and 3.41 times greater than TiO$_2$ and B-TiO$_2$ respectively, at 0.02007 min^{-1}. In addition, recycling performance is an important index to evaluate catalyst. The corresponding cyclic stability investigation of Au/B-TiO$_2$-2 is shown in Fig. 8d. After three cycles, there is only a slight decline, no significant decline, showing good stability. To assess the consequence of the effect of Gatifloxacin concentrations on the photocatalytic performance, experiments were conducted and the results are presented in Fig. S3.† The degradation performance was observed to be 73.8% when the Gatifloxacin concentration increased to 15 mg L^{-1}, which is likely due to the Gatifloxacin molecules covering the active sites, thus hindering the catalytic reaction. All the above-mentioned results show that Au/B-TiO$_2$ system is a kind of photocatalytic nanomaterial with high activity and stability.

3.5 Investigations of decomposition pathways

Furthermore, in order to understand the possible decomposition pathways of Gatifloxacin during the degradation process, the LC-MS technique was used to help us identifying the

intermediate products. The MS spectra of intermediates are revealed in Fig. S4–S7.† It can be found that the main m/z corresponding values from large to small are 376, 301, 282, 279, 266, 261, 244, 228, 205, 203, 101, 87, and 74. By analysing the intermediates, Fig. 9 displays three possible photodecomposition pathways of Gatifloxacin; these include demethylation, decarboxylation, deoxygenation, dehydroxylation, hydroxylation, benzene ring breakage, piperazine ring breakage and defluorination.[12]

As shown in Fig. 9, at the start of pathway I, P0 ($m/z = 376$) underwent a series of reactions such as demethylation, dehydroxylation, and defluorination to form P1 ($m/z = 301$). Then, P2 ($m/z = 279$) was created by demethylation, hydroxylation, benzene ring cleavage, dehydroxylation, and deoxygenation of P1. Subsequently, P3 ($m/z = 261$) was produced by dehydroxylation of P2. For pathway II, the reaction began with P0 forming P4 ($m/z = 282$) through a series of reactions including piperazine ring breakage, demethylation, hydroxylation, dehydroxylation, and benzene ring breakage. P5 ($m/z = 266$) was then obtained through dehydroxyl and demethyl hydroxylation. Following this, P5 was subjected to demethylation, defluorination, and dehydroxylation, resulting htr in the production of P6 ($m/z = 205$). On pathway III, P1 experienced piperazine ring cleavage, dehydroxylation, deoxygenation, defluorination, and hydroxylation to generate P7 ($m/z =$
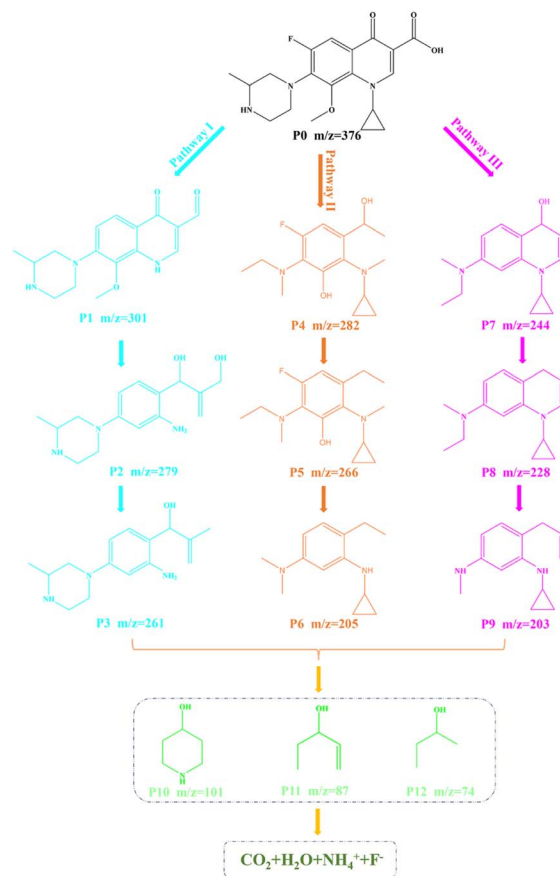

Fig. 9 Possible decomposition pathways of Gatifloxacin.

244). After demethylation of P7, P8 with an m/z of 228 was formed. P9 ($m/z = 203$) was then obtained by demethylation and breaking of the benzene ring of P8. Further reactions yielded a variety of small molecule structure intermediates, such as $m/z = 101$, 87, and 74. These results show that macromolecules are gradually broken down, and some of them eventually mineralize to produce H_2O, CO_2, F^-, and NH_4^+.

In addition, the mineralization performance of Au/B-TiO$_2$-2 was evaluated by TOC removal rate, which was calculated as 66.7% (Fig. S8†) by comparing the $TOC_{[final]}$ and $TOC_{[initial]}$.

3.6 Photocatalytic mechanism analysis

Capturing free radicals was the method used in experiments to investigate the different active groups in the photodegradation process. It is well known that $\cdot OH$, $\cdot O_2^-$ and h^+ are the main active groups in photocatalytic reactions.[42–44] In this study, EDTA–2Na, BQ and IPA were chosen as trapping agents for $\cdot OH$, $\cdot O_2^-$ and h^+, respectively.[45] Adding EDTA–2Na, BQ and IPA resulted in the degradation efficiency of Gatifloxacin dropping

Fig. 10 (a) Free radical capture in Au/B-TiO$_2$ system. (b) EPR of DMPO−$\cdot$OH. (c) And DMPO−$\cdot O_2^-$.

from 95.0% to 78.6%, 59.5% and 54.8%, respectively, as seen in Fig. 10a. It is evident from these results that these three free radicals influence the photodegradation of Gatifloxacin. Furthermore, $\cdot OH$ and $\cdot O_2^-$ have a greater effect than h^+. Notably, $\cdot OH$ has the most powerful influence as it has multiple sources and can be involved in photocatalytic reactions to remove Gatifloxacin. This is because a portion of $\cdot OH$ is created from the interaction of h^+ with adsorbed H_2O or OH^-.[46] In addition, $\cdot OH$ may be generated from the reaction between H_2O_2 and $\cdot O_2^-$.[47]

The ESR technique was used to analyse the presence of $\cdot OH$ and $\cdot O_2^-$ during photodegradation. As seen in Fig. 10b and c, no signal was detected in the dark state (0 min). After 5 min of light exposure, a quadruple peak of $\cdot OH$ was observed ($1 : 2 : 2 : 1$), confirming its presence (Fig. 10b). At the same time, four ESR peaks with a $1 : 1 : 1 : 1$ area ratio was observed, implying the presence of $\cdot O_2^-$ (Fig. 10c). With the extension of the irradiation time to 10 min, the ESR signals grew stronger, indicating an augmentation in the formation of free radicals.

Generally speaking, when the light used to stimulate a semiconductor catalyst has an energy that is higher than the E_g of the semiconductor, photogenerated holes and electrons are formed. These holes and electrons create active groups that are involved in the breakdown of pollutants. To determine the energy level of the valence band and conductive band for each component, the Mott–Schottky technique was used. As is demonstrated in Fig. S9,† which shows a flat band potential (E_{fb}) of B-TiO$_2$ is −0.30 V $vs.$ Ag/AgCl. According to eqn (1), E_{fb} of B-TiO$_2$ was estimated to be −0.10 V $vs.$ NHE.[48]

$$E_{NHE} = E_{Ag/AgCl} + 0.197 \tag{1}$$

Generally, TiO$_2$ is an n-type semiconductor and its conduction band potential (E_{CB}) is 0.20 eV positive than its E_{fb}.[49] Hence, the E_{CB} of B-TiO$_2$ was calculated to −0.30 V $vs.$ NHE. Base on eqn (2) and E_g value (Fig. 5b), the valence band potential (E_{VB}) of B-TiO$_2$ was determined to be 2.68 V $vs.$ NHE,

$$E_g = E_{VB} - E_{CB} \tag{2}$$

In addition, on the basis of the outcomes of the prior investigation, the Fermi level (E_f) of Au was 0.81 V $vs.$ NHE.[39]

According to the above results, the mechanism insight and the photodegradation process of Gatifloxacin by Au/B-TiO$_2$ system are illustrated in Fig. 11. When exposed to light radiation, high energetic electrons created by the SPR of Au will be moved to the conduction band of B-TiO$_2$.[50] Meanwhile, electrons and holes were produced at the conduction band and valence band of B-TiO$_2$ under ultraviolet excitation, respectively. Since $O_2/\cdot O_2^-$ (−0.046 V $vs.$ NHE) has a higher potential than B-TiO$_2$'s E_{CB} (−0.30 V $vs.$ NHE), electrons at conduction band of B-TiO$_2$ are able to react with O_2 to form $\cdot O_2^-$ (eqn (4)).[51] Additionally, since the E_{VB} of B-TiO$_2$ (2.68 V $vs.$ NHE) is more positive than that of $H_2O/\cdot OH$ (2.37 V $vs.$ NHE) and $OH^-/$ $\cdot OH$ (1.99 V $vs.$ NHE). Therefore, interaction between H_2O and OH^- and the photogenerated holes of B-TiO$_2$ leads to the production of $\cdot OH$ (eqn (5) and (6)).[52,53] Eventually,
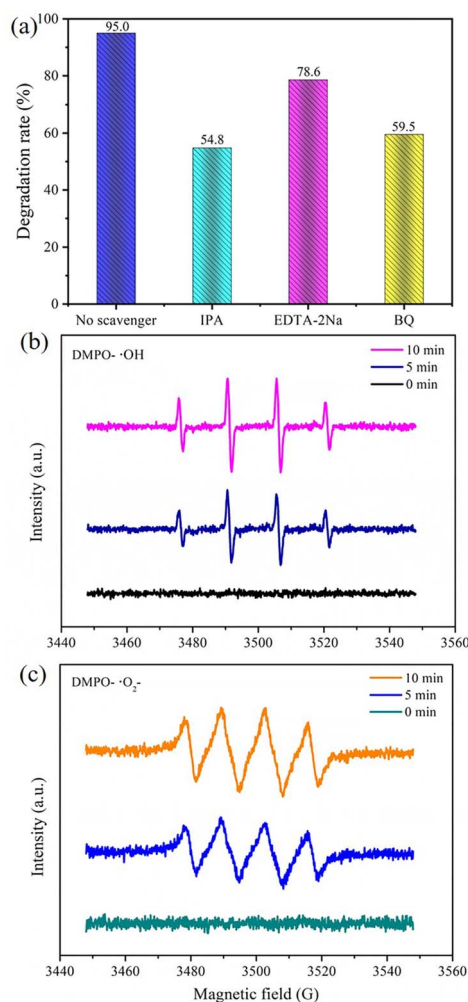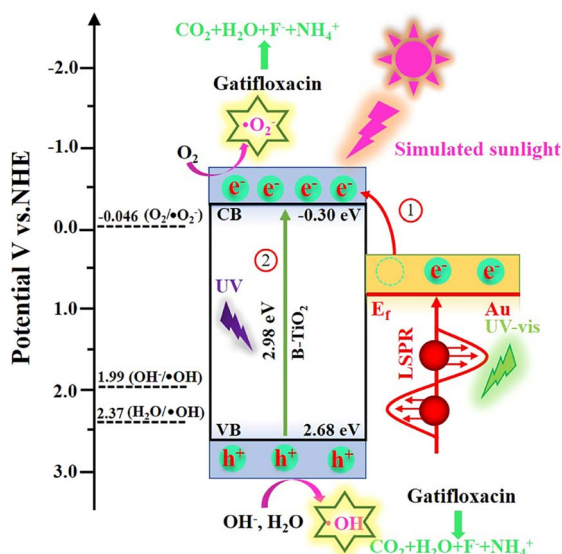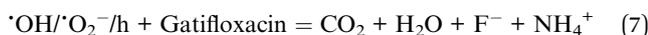
Fig. 11 Mechanism for Gatifloxacin decomposition by Au/B-TiO$_2$ system.

Gatifloxacin will be gradually degraded under the action of $^\bullet$OH, $^\bullet$O$_2^-$ and h$^+$, eventually becoming H$_2$O, CO$_2$, F$^-$, and NH$_4^+$ (eqn (7)).

$$Au/B\text{-}TiO_2 + h\nu = Au/B\text{-}TiO_2\ (e^- + h^+) \quad (3)$$

$$e^- + (O_2)_{abs} = {}^\bullet O_2^- \quad (4)$$

$$h^+ + H_2O = {}^\bullet OH + H^+ \quad (5)$$

$$h^+ + OH^- = {}^\bullet OH \quad (6)$$

$${}^\bullet OH/{}^\bullet O_2^-/h + Gatifloxacin = CO_2 + H_2O + F^- + NH_4^+ \quad (7)$$

4. Conclusions

In this work, an effective heterostructure catalyst composed of Au nanoparticles sensitized blue TiO$_2$ nanorods arrays (Au/B-TiO$_2$) was developed for the removal of Gatifloxacin. The photocatalytic removal ability of this catalyst was proven to be highly efficient with a maximum efficiency of 95.0% and a reaction constant K_α of 0.02007 min^{-1}. Three possible photodegradation pathways of Gatifloxacin were proposed. The remarkable photocatalytic performance of Au/B-TiO$_2$ is a result of combined effect of its each component, such as the TiO$_2$ nanorod arrays which serve as efficient transfer channels and provide a larger surface area for Au deposition, the presence of oxygen vacancies in blue TiO$_2$ nanorod arrays which enhance the catalytic activity, the surface plasmon resonance (SPR) effect of Au which generates high-energy hot electrons, and the improvement of light capture capability. This research presents a successful approach for the production of highly efficient photocatalysts, which can improve the light absorption capacity, promote the efficient separation of photogenerated carriers, and significantly improve the photocatalytic performance.

Author contributions

Jun Guo: conceptualization, methodology, investigation, data curation, and writing–original draft. Wei Gan: investigation, and methodology. Ruixin Chen: data curation. Miao Zhang: funding acquisition, and resources. Zhaoqi Sun: supervision, project administration, and funding acquisition.

Conflicts of interest

There are no conflicts to declare.

Acknowledgements

Notes and references

1 A. Arjyal, B. Basnyat, H. T. Nhan, S. Koirala, A. Giri, N. Joshi, M. Shakya, K. R. Pathak, S. P. Mahat, S. P. Prajapati, N. Adhikari, R. Thapa, L. Merson, D. Gajurel, K. Lamsal, D. Lamsal, B. K. Yadav, G. Shah, P. Shrestha, S. Dongol, A. Karkey, C. N. Thompson, N. T. V. Thieu, D. P. Thanh, S. Baker, G. E. Thwaites, M. Wolbers and C. Dolecek, Lancet Infect. Dis., 2016, 16, 535–545.
2 M. Li, J.-W. Xu, J. Li, W. Wang, C. Luo, H. Han, Z.-K. Xu and K. Yao, Bioact. Mater., 2023, 20, 271–285.
3 F. Huang, Z. An, M. J. Moran and F. Liu, J. Hazard. Mater., 2020, 399, 122813.
4 K. Wang, X. Yang and Y. Pei, J. Cleaner Prod., 2023, 409, 137125.
5 J. Yan, L. Gong, S. Chai, C. Guo, W. Zhang and H. Wan, Sep. Purif. Technol., 2022, 302, 122016.
6 Q. Zhang, J. Chen, X. Gao, H. Che, P. Wang and Y. Ao, Appl. Catal., B, 2022, 313, 121443.
7 F. Chang, Y. Xie, J. Zhang, J. Chen, C. Li, J. Wang, J. Luo, B. Deng and X. Hu, RSC Adv., 2014, 4, 28519–28528.
8 Z. Xing, J. Zhang, J. Cui, J. Yin, T. Zhao, J. Kuang, Z. Xiu, N. Wan and W. Zhou, Appl. Catal., B, 2018, 225, 452–467.
9 S. Peiris, H. B. Silva, K. N. Ranasinghe, S. V. Bandara and I. R. Perera, J. Chin. Chem. Soc., 2021, 68, 738–769.
10 Y. Wei, Q. Wu, H. Meng, Y. Zhang and C. Cao, RSC Adv., 2023, 13, 20584–20597.
11 T. H. A. Nguyen, D. T. Quang, L. V. Tan and T. K. Vo, RSC Adv., 2023, 13, 5859–5868.
12 W. Gan, J. Guo, X. Fu, J. Jin, M. Zhang, R. Chen, C. Ding, Y. Lu, J. Li and Z. Sun, Sep. Purif. Technol., 2023, 317, 123791.
13 Q. Zhu, Y. Peng, L. Lin, C.-M. Fan, G.-Q. Gao, R.-X. Wang and A.-W. Xu, J. Mater. Chem. A, 2014, 2, 4429–4437.
14 R. Wang, R. Jiang, C. Dong, T. Tong, Z. Li, H. Liu and X.-W. Du, Ind. Eng. Chem. Res., 2021, 60, 273–280.
15 A. Davó-Quiñonero, E. Bailón-García, S. López-Rodríguez, J. Juan-Juan, D. Lozano-Castelló, M. García-Melchor,

F. C. Herrera, E. Pellegrin, C. Escudero and A. Bueno-López, *ACS Catal.*, 2020, **10**, 6532–6545.

16 Y. Chen, L. Wang, R. Gao, Y.-C. Zhang, L. Pan, C. Huang, K. Liu, X.-Y. Chang, X. Zhang and J.-J. Zou, *Appl. Catal., B*, 2019, **259**, 118079.

17 S. Wu, M. Y. Manuputty, Y. Sheng, H. Wang, Y. Yan, M. Kraft and R. Xu, *Small Methods*, 2021, **5**, 2000928.

18 Z. Hao, Q. Chen, W. Dai, Y. Ren, Y. Zhou, J. Yang, S. Xie, Y. Shen, J. Wu, W. Chen and G. Q. Xu, *Adv. Energy Mater.*, 2020, **10**, 1903107.

19 L. Liao, M. Wang, Z. Li, X. Wang and W. Zhou, *Nanomaterials*, 2023, **13**, 468.

20 J. Cai, M. Zhou, X. Du and X. Xu, *Sep. Purif. Technol.*, 2021, **254**, 117560.

21 A. Martinez-Oviedo, S. K. Ray, H. P. Nguyen and S. W. Lee, *J. Photochem. Photobiol., A*, 2019, **370**, 18–25.

22 D. P. Kumar, A. P. Rangappa, H. S. Shim, K. H. Do, Y. Hong, M. Gopannagari, K. A. J. Reddy, P. Bhavani, D. A. Reddy, J. K. Song and T. K. Kim, *Mater. Today Chem.*, 2022, **24**, 100827.

23 Y. Xu, R. Feng, M. Zhang, C. Yan, J. Liu, T. Zhang and X. Wang, *J. Environ. Sci.*, 2023, **126**, 590–601.

24 Y. Zhang, X. Xu, J. Cai, Y. Pan and M. Zhou, *Chemosphere*, 2021, **266**, 129063.

25 D. Lan, W. Sheng, Q. Fu and J. Ge, *Nano Res.*, 2023, **16**, 9310–9317.

26 S. Cai, J. Chen, Q. Li and H. Jia, *ACS Appl. Mater. Interfaces*, 2021, **13**, 14221–14229.

27 A. Meng, L. Zhang, B. Cheng and J. Yu, *Adv. Mater.*, 2019, **31**, 1807660.

28 A. Philip and A. R. Kumar, *Coord. Chem. Rev.*, 2022, **458**, 214424.

29 S. K. Md Saad, A. Ali Umar, M. I. Ali Umar, M. Tomitori, M. Y. A. Rahman, M. Mat Salleh and M. Oyama, *ACS Omega*, 2018, **3**, 2579–2587.

30 C. Li, T. Wang, Z. J. Zhao, W. Yang, J. F. Li, A. Li, Z. Yang, G. A. Ozin and J. Gong, *Angew. Chem., Int. Ed.*, 2018, **57**, 5278–5282.

31 K. Wang, M. Cao, J. Lu, Y. Lu, C. H. Lau, Y. Zheng and X. Fan, *Appl. Catal., B*, 2021, **296**, 120341.

32 N. Celebi, M. Y. Aydin, F. Soysal, Y. O. Ciftci and K. Salimi, *J. Alloys Compd.*, 2021, **860**, 157908.

33 K. Wang, K. Yoshiiri, L. Rosa, Z. Wei, S. Juodkazis, B. Ohtani and E. Kowalska, *Catal. Today*, 2022, **397–399**, 257–264.

34 J. W. Gregory, Y. Gong, Y. Han, S. Huband, R. I. Walton, V. Hessel and E. V. Rebrov, *Catal. Today*, 2023, **418**, 114145.

35 Y. Qin, Y. Guo, Z. Liang, Y. Xue, X. Zhang, L. Yang and J. Tian, *Chin. Chem. Lett.*, 2021, **32**, 1523–1526.

36 Y. Lu, C. Ding, J. Guo, W. Gan, P. Chen, M. Zhang and Z. Sun, *J. Alloys Compd.*, 2022, **924**, 166533.

37 Y. Yu, X. a. Dong, P. Chen, Q. Geng, H. Wang, J. Li, Y. Zhou and F. Dong, *ACS Nano*, 2021, **15**, 14453–14464.

38 A. Wang, S. Wu, J. Dong, R. Wang, J. Wang, J. Zhang, S. Zhong and S. Bai, *Chem. Eng. J.*, 2021, **404**, 127145.

39 J. Guo, C. Ding, W. Gan, P. Chen, Y. Lu, J. Li, R. Chen, M. Zhang and Z. Sun, *Sep. Purif. Technol.*, 2023, **307**, 122838.

40 B. Kim, N. Lee, S. Park, T. Park, J. Song, S. Han, H. Park, D. Lee, H. Kim and H. Jeon, *J. Alloys Compd.*, 2021, **857**, 157931.

41 D. Dahlan, S. K. Md Saad, A. U. Berli, A. Bajili and A. A. Umar, *Phys. E*, 2017, **91**, 185–189.

42 F. Chang, B. Lei, C. Yang, J. Wang and X. Hu, *Chem. Eng. J.*, 2021, **413**, 127443.

43 G. Liao, Y. Gong, L. Zhang, H. Gao, G.-J. Yang and B. Fang, *Environ. Sci. Technol.*, 2019, **12**, 2080–2147.

44 G. Liao, C. Li, X. Li and B. Fang, *Cell Rep. Phys. Sci.*, 2021, **2**, 100355.

45 J. Guo, W. Gan, C. Ding, Y. Lu, J. Li, S. Qi, M. Zhang and Z. Sun, *Sep. Purif. Technol.*, 2022, **297**, 121454.

46 S. Wu, H. Hu, Y. Lin, J. Zhang and Y. H. Hu, *Chem. Eng. J.*, 2020, **382**, 122842.

47 H. Kim, J. Lim, S. Lee, H.-H. Kim, C. Lee, J. Lee and W. Choi, *Environ. Sci. Technol.*, 2019, **53**, 2918–2925.

48 J. Yang, L. Li, F. Fu, H. Xu, K. Da, S. Cao, W. Chen, L. Yang and X. Fan, *Appl. Surf. Sci.*, 2023, **610**, 155598.

49 Z. Yang, X. Xia, L. Shao, L. wang and Y. Liu, *Chem. Eng. J.*, 2021, **410**, 128454.

50 D. Wibowo, M. Z. Muzakkar, S. K. M. Saad, F. Mustapa, M. Maulidiyah, M. Nurdin and A. A. Umar, *J. Photochem. Photobiol., A*, 2020, **398**, 112589.

51 J. S. Adams, A. Chemburkar, P. Priyadarshini, T. Ricciardulli, Y. Lu, V. Maliekkal, A. Sampath, S. Winikoff, A. M. Karim, M. Neurock and D. W. Flaherty, *Science*, 2021, **371**, 626–632.

52 B. He, Z. Wang, P. Xiao, T. Chen, J. Yu and L. Zhang, *Adv. Mater.*, 2022, **34**, e2203225.

53 Y. G. Kim and W. K. Jo, *J. Hazard. Mater.*, 2019, **361**, 64–72.